ELSEVIER

The effect of creep flow on two-dimensional isoflux microchannels

Jennifer van Rij, Todd Harman, Timothy Ameel *

Department of Mechanical Engineering, University of Utah, Salt Lake City, UT 84112, USA

Abstract

Microchannel convective heat transfer and friction loss characteristics are numerically evaluated for gaseous, two-dimensional, steady state, laminar, constant wall heat flux flows. The effects of Knudsen number, accommodation coefficients, second-order slip boundary conditions, creep flow, and hydrodynamically/thermally developing flow are considered. These effects are compared through the Poiseuille number and the Nusselt number. Numerical values for the Poiseuille and Nusselt numbers are obtained using a continuum based three-dimensional, unsteady, compressible computational fluid dynamics algorithm that has been modified with slip boundary conditions. To verify the numerical results, analytic solutions of the hydrodynamically and thermally fully developed momentum and energy equations have been derived subject to both first- and second-order slip velocity and temperature jump boundary conditions. The resulting velocity and temperature profiles are then utilized to obtain the microchannel Poiseuille and Nusselt numbers as a function of Knudsen number, first- and second-order velocity slip and temperature jump coefficients, Brinkman number, and the ratio of the thermal creep velocity to the mean velocity. Excellent agreement between the numerical and analytical data is demonstrated. Second-order slip terms and creep velocity are shown to have significant effects on microchannel Poiseuille and Nusselt numbers within the slip flow regime.
© 2007 Elsevier Masson SAS. All rights reserved.

Keywords: Microchannel; Slip; Creep; Viscous dissipation; Nusselt number; Poiseuille number

1. Introduction

Convective heat transfer and friction losses of gaseous microchannel flows are important due to their applications in microscale heat exchangers, sensors, reactors, power systems, etc. However, due to measurement and accuracy limitations there are currently no experimental data on convective heat transfer rates of gaseous microchannel flows in the slip regime. For this reason, accurate numerical models, verified by analytical solutions, are particularly important in the process of understanding and designing these microfluidic systems.

Numerous studies on microchannel convective heat transfer in the slip flow regime for both constant wall temperature and constant wall heat flux have been conducted. The majority of these studies have been analytical [1–8], although there are also several numerical studies based on either direct simulation Monte Carlo, DSMC [9–11], or on continuum methods with slip boundary conditions [12,13]. Nearly all of these studies have used the following simplifying assumptions: laminar, steady state, hydrodynamically fully developed, constant properties, no creep flow, and first-order accurate slip velocity and temperature jump boundary conditions with perfectly accommodating walls. Parameters that have been found to affect microchannel heat transfer rates and friction losses include the Knudsen number, the momentum and thermal accommodation coefficients, channel aspect ratio, compressibility, viscous dissipation, and the Peclet number. However, many of the simplifying assumptions and conclusions of these studies have not yet been verified numerically or experimentally, nor have the effects of creep, second-order accurate slip boundary conditions, or combined hydrodynamic/thermal flow development been fully investigated.

Theoretical studies within the slip flow regime ($0.01 \leqslant Kn \leqslant 0.1$) typically use the continuum momentum and energy equations with the slip boundary conditions shown in Eqs. (1) and (2) to account for rarefaction effects. The velocity slip boundary condition, Eq. (1), was first introduced by

---

* Corresponding author. Tel.: +1 801 585 9730; fax: +1 801 585 9826.
  E-mail address: ameel@mech.utah.edu (T. Ameel).

Nomenclature

Br	Brinkman number, $\mu u_m^2/q_o'' D_h$
c_p	specific heat at constant pressure .... $\mathrm{J\,kg^{-1}\,K^{-1}}$
D_h	hydraulic diameter, $2h$ .... m
f	friction factor, $8\tau_w/\rho u_m^2$
h	channel height .... m
k	thermal conductivity .... $\mathrm{W\,m^{-1}\,K^{-1}}$
Kn	Knudsen number, λ/D_h
Ma	Mach number, $u/\sqrt{kRT}$
Nu	Nusselt number, $q_o'' D_h/k(T_w - T_m)$
P	fluid pressure .... Pa
Pe	Peclet number, $Pr \cdot Re$
Po	Poiseuille number, $f \cdot Re$
Pr	Prandtl number, $c_p \mu/k$
q_o''	wall heat flux, $-k\partial T/\partial y\vert_{y=0}$ .... $\mathrm{W\,m^{-2}}$
R	gas constant .... $\mathrm{J\,kg^{-1}\,K^{-1}}$
Re	Reynolds number, $\rho u_m D_h/\mu$
T	fluid temperature .... K
T_m	mixed mean temperature,
	$(1/hu_m)\int_0^h u(y) \cdot T(y)\,\mathrm{d}y$ .... K
T_w	wall temperature .... K
u	streamwise velocity .... $\mathrm{m\,s^{-1}}$

u_c	creep velocity, $(3/4)(\mu/\rho T_w)\partial T/\partial x\vert_{y=0}$ .. $\mathrm{m\,s^{-1}}$
u_m	mean velocity, $(1/h)\int_0^h u(y)\,\mathrm{d}y$ .... $\mathrm{m\,s^{-1}}$
u_s	slip velocity, $u\vert_{y=0}$ .... $\mathrm{m\,s^{-1}}$
x, y, z	Cartesian coordinates .... m

Greek symbols

α	thermal diffusivity, $k/\rho c_p$ .... $\mathrm{m^2\,s^{-1}}$
β_{T1}	first-order temperature jump coefficient,
	$((2 - \sigma_T)/\sigma_T)(2\gamma/(\gamma + 1))(1/Pr)$
β_{T2}	second-order temperature jump coefficient
β_{V1}	first-order velocity slip coefficient, $(2 - \sigma_V)/\sigma_V$
β_{V2}	second-order velocity slip coefficient
ε	relative error
γ	ratio of specific heat capacities
λ	molecular mean free path, $\mu/\rho\sqrt{2RT_w/\pi}$ .... m
μ	viscosity .... $\mathrm{kg\,m^{-1}\,s^{-1}}$
ρ	density .... $\mathrm{kg\,m^{-3}}$
σ_T	thermal accommodation coefficient
σ_V	momentum accommodation coefficient
τ_w	wall shear stress, $\mu\partial u/\partial y\vert_{y=0}$ .... Pa

Maxwell [14], and the temperature jump boundary condition, Eq. (2), was originally proposed by Smoluchowski [15].

$$u\vert_{y=0} = \left(\frac{2 - \sigma_V}{\sigma_V}\right)\lambda\frac{\partial u}{\partial y}\bigg\vert_{y=0} + \frac{3}{4}\frac{\mu}{\rho T_w}\frac{\partial T}{\partial x}\bigg\vert_{y=0} \quad (1)$$

$$T\vert_{y=0} - T_w = \left(\frac{2 - \sigma_T}{\sigma_T}\right)\left(\frac{2\gamma}{\gamma + 1}\right)\frac{\lambda}{Pr}\frac{\partial T}{\partial y}\bigg\vert_{y=0} \quad (2)$$

Values for the momentum and thermal accommodation coefficients range from 0 to 1, where these values represent complete specular and diffuse reflections, respectively. The first term in Eq. (1) is the velocity slip due to the wall shear stress, and the second term is the thermal creep velocity, u_c, due to the streamwise temperature gradient. Eqs. (1) and (2) are first-order approximations, in Kn, and only applicable in the slip flow regime. However, in an effort to improve the slip flow model, and extend the continuum equations' range of applicability into the transition regime ($0.1 \leqslant Kn \leqslant 1.0$), several second-order slip boundary condition models have been proposed. The boundary conditions derived by Deissler [16] are given in Eqs. (3) and (4), and the boundary conditions suggested by Karniadakis and Beskok [17] are given in Eqs. (5) and (6).

$$u\vert_{y=0} = \left(\frac{2 - \sigma_V}{\sigma_V}\right)\lambda\frac{\partial u}{\partial y}\bigg\vert_{y=0}$$
$$- \frac{9\lambda^2}{8}\left[\frac{\partial^2 u}{\partial y^2} + \frac{1}{2}\frac{\partial^2 u}{\partial x^2} + \frac{1}{2}\frac{\partial^2 u}{\partial z^2}\right]_{y=0} + u_c \quad (3)$$

$$T\vert_{y=0} - T_w = \left(\frac{2 - \sigma_T}{\sigma_T}\right)\left(\frac{2\gamma}{\gamma + 1}\right)\frac{\lambda}{Pr}\frac{\partial T}{\partial y}\bigg\vert_{y=0}$$

$$- \frac{9\lambda^2}{128}\left(\frac{177\gamma - 145}{\gamma + 1}\right)$$
$$\times \left[\frac{\partial^2 T}{\partial y^2} + \frac{1}{2}\frac{\partial^2 T}{\partial x^2} + \frac{1}{2}\frac{\partial^2 T}{\partial z^2}\right]_{y=0} \quad (4)$$

$$u\vert_{y=0} = \left(\frac{2 - \sigma_V}{\sigma_V}\right)\left[\lambda\frac{\partial u}{\partial y} + \frac{\lambda^2}{2}\frac{\partial^2 u}{\partial y^2}\right]_{y=0} + u_c \quad (5)$$

$$T\vert_{y=0} - T_w = \left(\frac{2 - \sigma_T}{\sigma_T}\right)\left(\frac{2\gamma}{\gamma + 1}\right)\frac{1}{Pr}\left[\lambda\frac{\partial T}{\partial y} + \frac{\lambda^2}{2}\frac{\partial^2 T}{\partial y^2}\right]_{y=0} \quad (6)$$

In addition to these two sets of boundary conditions, many other second-order boundary conditions have been proposed for the slip velocity, without a complimentary temperature jump boundary condition, and so will not be considered here. Although there is currently no consensus on which set of second-order boundary conditions is most accurate, it has been shown experimentally that the use of second-order boundary conditions does extend the range of the continuum approach when modeling microchannel mass flow rates [17–19]. For this reason, it is important that the effects of second-order slip boundary conditions on convective heat transfer be evaluated as well.

This study will analytically and numerically evaluate two-dimensional microchannel flows with constant wall heat flux using the continuum conservation equations and the various forms of the slip boundary condition models presented in Eqs. (1)–(6). The effects of Knudsen number, accommodation coefficients, and creep flow on microchannel friction losses and convective heat transfer will be evaluated numerically through the Poiseuille number, Po, and the Nusselt number, Nu. To val-

idate the numerical model, analytic solutions for the hydrodynamically and thermally fully developed values of Po and Nu, which include the effects of second-order slip boundary conditions, creep velocity, and viscous dissipation, will be derived. With the numerical method verified, it will then be used to evaluate the thermally and hydrodynamically developing flows considered in this study, as well as more complex geometries and heating configurations in future studies.

2. Analytic solution

The flow configuration for the analytical model is shown in Fig. 1. The following simplifying assumptions are applied: two-dimensional, steady state, incompressible, thermally and hydrodynamically fully developed, symmetrically isoflux, Newtonian, ideal gas, constant properties, and laminar flow. With these simplifications the momentum equation takes the form

$$\frac{\partial^2 u}{\partial y^2} = \frac{1}{\mu}\frac{dP}{dx} \tag{7}$$

and the energy equation is

$$\frac{\partial^2 T}{\partial y^2} = \frac{u}{\alpha}\frac{\partial T}{\partial x} - \frac{u}{k}\frac{\partial P}{\partial x} - \frac{\mu}{k}\left(\frac{\partial u}{\partial y}\right)^2 \tag{8}$$

where both the pressure and temperature gradients in the x-direction are constants.

For two-dimensional, fully developed, planar flow all three sets of slip boundary conditions, Eqs. (1)–(6), may be written in the forms

$$u|_{y=0} = \left[\beta_{V1}\lambda\frac{\partial u}{\partial y} - \beta_{V2}\lambda^2\frac{\partial^2 u}{\partial y^2}\right]_{y=0} + u_c \tag{9}$$

$$T|_{y=0} = T_w + \left[\beta_{T1}\lambda\frac{\partial T}{\partial y} - \beta_{T2}\lambda^2\frac{\partial^2 T}{\partial y^2}\right]_{y=0} \tag{10}$$

Values for the first-order slip coefficient, β_{V1}, are typically near unity while values for the first-order jump coefficient, β_{T1}, may range from 0 to 100. The second-order slip and jump coefficients, β_{V2} and β_{T2}, vary depending on the model selected and are given in Table 1.

Using the general form of the slip velocity boundary condition, Eq. (9), and symmetry at the microchannel midplane, the momentum equation, Eq. (7), may be integrated twice to obtain the nondimensional velocity profile.

$$\frac{u(y)}{u_m} = \frac{u_s}{u_m} + 6\left(1 - \frac{u_s}{u_m}\right)\left(\frac{y}{h} - \frac{y^2}{h^2}\right) \tag{11}$$
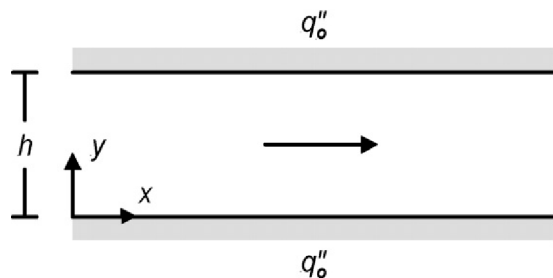

Fig. 1. Flow configuration.

Table 1
Second-order velocity slip and temperature jump coefficients

	First-order [14,15]	Second-order [16]	Second-order [17]
β_{V2}	0	$\frac{9}{8}$	$-\frac{\beta_{V1}}{2}$
β_{T2}	0	$\frac{9}{128}(\frac{1//\gamma - 145}{\gamma+1})$	$-\frac{\beta_{T1}}{2}$

Where u_s/u_m is defined as

$$\frac{u_s}{u_m} = 1 - \frac{(1 - u_c/u_m)}{(1 + 12\beta_{V1}Kn + 48\beta_{V2}Kn^2)} \tag{12}$$

The ratio u_c/u_m may be calculated based on the known mass flow rate, the flow properties, and the wall heat flux. With the velocity profile defined, the Poiseuille number may be expressed as

$$Po = 96\left(1 - \frac{u_s}{u_m}\right) \tag{13}$$

The velocity profile, Eq. (11), is substituted into the energy equation, Eq. (8), which is then integrated twice. The general form of the temperature jump boundary condition, Eq. (10), and symmetry at the midplane, are then applied to obtain the nondimensional temperature profile.

$$\frac{T_w - T(y)}{q_o'' D_h/k}$$

$$= \left(\frac{1}{2}\right)\left(\frac{y}{h} - \frac{y^2}{h^2}\right)\left\{1 + \left[1 + 12Br\left(3 - \frac{u_s}{u_m}\right)\left(1 - \frac{u_s}{u_m}\right)\right]\right.$$

$$\times \left(1 - \frac{u_s}{u_m}\right)\left(\frac{y}{h} - \frac{y^2}{h^2}\right)\right\} + \beta_{T1}Kn + 4\beta_{T2}Kn^2$$

$$\times \left[\frac{u_s}{u_m} - 12Br\left(3 - \frac{u_s}{u_m}\right)\left(1 - \frac{u_s}{u_m}\right)^2\right] \tag{14}$$

Where the Brinkman number, Br, represents the effects of viscous dissipation. Using the temperature profile in Eq. (14) and the definitions of the mixed mean temperature, T_m, and the Nusselt number, Nu, the final form for the Nusselt number is

$$Nu = 420\left[51 + 420\beta_{T1}Kn - 2\frac{u_s}{u_m}\left(9 - \frac{u_s}{u_m} - 840\beta_{T2}Kn^2\right)\right.$$

$$+ 12Br\left(3 - \frac{u_s}{u_m}\right)\left(1 - \frac{u_s}{u_m}\right)^2$$

$$\times \left.\left(9 - 2\frac{u_s}{u_m} - 1680\beta_{T2}Kn^2\right)\right]^{-1} \tag{15}$$

Nu presented in Eq. (15), with u_s/u_m defined in Eq. (12), expresses the thermal energy exchange of a two-dimensional, fully developed, isoflux microchannel in terms of the degree of rarefaction (Kn); slip flow model parameters, β_{V1}, β_{V2}, β_{T1}, and β_{T2}; creep flow (u_c/u_m); and viscous dissipation (Br). For continuum flow ($Kn = 0$), with negligible viscous dissipation ($Br = 0$), Eq. (15) reduces to the continuum value of 8.235. For continuum flow, with viscous dissipation, Eq. (15) reduces to the Nu equation given in [20] for flow with viscous dissipation. For slip flow with no viscous dissipation, no creep flow ($u_c/u_m = 0$), and first-order slip terms only ($\beta_{V2} = \beta_{T2} = 0$),

Eq. (15) reduces to the equation originally derived by Inman [17] (with $Kn = \lambda/h$, rather than $Kn = \lambda/2h$ used here). Although it is expected that these solutions for Po and Nu, given by Eqs. (13) and (15) respectively, are more accurate than first-order models and models that do not include creep and viscous dissipation effects they are still only applicable to situations of approximately the same conditions for which the solutions were derived, that is two-dimensional, isoflux, nearly incompressible, constant property flows within the slip flow regime.

3. Computational model

The computational fluid dynamics (CFD) algorithm used in this study is based on the ICE (Implicit, Continuous-fluid Eulerian) method. ICE is a finite volume, multi-material CFD algorithm that originated [21], and was subsequently developed, at Los Alamos National Laboratory [22]. The ICE implementation used in this study is well developed and documented [23–25]. The code is three-dimensional, fully compressible, unsteady, and capable of modeling variable fluid properties, fluid-structure interactions, and chemical reactions. Although, the present study will not use the majority of the algorithms described capabilities, it has been selected for several reasons. First, by developing and verifying the algorithm's capability to model slip flow in this study, it may then be used in future studies for more complicated microscale flows which utilize the code's more advanced capabilities and would consequently not be feasible with most commercial CFD algorithms. Second, as an 'open' research code it is very flexible in comparison to commercial codes and relatively easy to make customized changes to, such as second-order slip boundary conditions. And finally, when using this code there is significant computing power and expertise available where the study is performed.

To accurately model microchannel flows using this algorithm, several additional capabilities have been implemented and verified. These modifications include slip flow with creep velocity boundary conditions, temperature jump boundary conditions, and viscous dissipation. The implementation of these modifications is consistent with the existing code in being numerically second-order accurate both spatially and temporally. Any form of the slip boundary conditions presented in Eqs. (1)–(6) may be numerically employed. Also, any of these modifications may be either included or neglected with each calculation, such that each contribution to the numerical result may be observed.

3.1. Model parameters and solution criteria

To decrease the computational time required to reach a solution only half of the symmetric microchannel, shown in Fig. 1, is modeled. Two types of problems are numerically evaluated, thermally developing flows and combined hydrodynamically/thermally developing flows. For both cases the channel outlet pressure is specified to obtain the desired flow Kn. For thermally developing flows, the inlet pressure is specified to

obtain the desired flow Pe, while the inlet and outlet velocities are allowed to evolve to their fully developed profiles. For hydrodynamically/thermally developing flows, a uniform inlet velocity is specified to obtain the desired flow Pe, while the inlet pressure and outlet velocity are allowed to evolve. For both cases, a uniform inlet temperature is specified while the outlet temperature is allowed to evolve to its fully developed profile; and a uniform heat flux boundary condition and slip velocity boundary condition, dependent on the flow Kn, are applied at the channel wall.

Because the algorithm is unsteady the flow properties must evolve from a set of initial conditions to steady state conditions subject to the boundary conditions. For all of the data presented, the initial velocity field is zero and the initial temperature field is equal to the inlet temperature. The magnitude and number of time steps required to reach steady state are dependent on the grid resolution, Kn, and Pe for each flow. The convergence criteria for each time step is a mass flux residual less than 10^{-8} for each control volume. The criterion used to establish that the flow is steady state is, $|(u^{n+1} - u^n)/u^{n+1}| \leqslant 10^{-10}$ and $|(T^{n+1} - T^n)/T^{n+1}| \leqslant 10^{-10}$, for each control volume, where n is the number of the time step.

For the numerical results to be comparable to the analytic solutions, the flow must be fully developed, steady state, nearly incompressible, and have constant properties. Given these stipulations, the flow Pe, and wall heat flux are specified to be small enough that the density and temperature changes within the flow are less than a few percent and the flow Mach number (Ma) is small. Using constant properties of air, $Pe = 0.5$, and $Kn = 0.01, 0.04$, and 0.12 the resulting $Ma = 0.005, 0.019$, and 0.056, respectively. For the Pe values used in this study a channel length of $3h$ was found to be sufficient for the parameters of interest, Po and Nu, to reach nearly constant, locally fully developed values while avoiding significant compressibility effects due to a longer channel. (Evidence of this statement will be seen shortly in the plots presented for developing Po and Nu in Figs. 2, and 9–12.)

3.2. Grid dependence

The resulting numerical velocity and temperature fields may be used to calculate Po and Nu along the length of the microchannel. The accuracy of the numerical solutions and the time required to reach a steady-state solution are dependent on the grid resolution. This is shown for thermally developing Nu with the conditions specified in Table 2 and Fig. 2. These data indicate that the numerical solution converges to the exact analytic solution with approximately second-order numerical accuracy, and that the solution is sufficiently accurate at the finest resolution that is practical due to computational time limitations. Grid dependence studies have been completed with similar results for each numerical solution presented in the results section, with only the results from the finest resolution (40×120 for each case) being presented. It may also be observed in Fig. 2, that as stated previously, Nu reaches a nearly constant, locally fully developed state well before the end of the channel at $3h$.
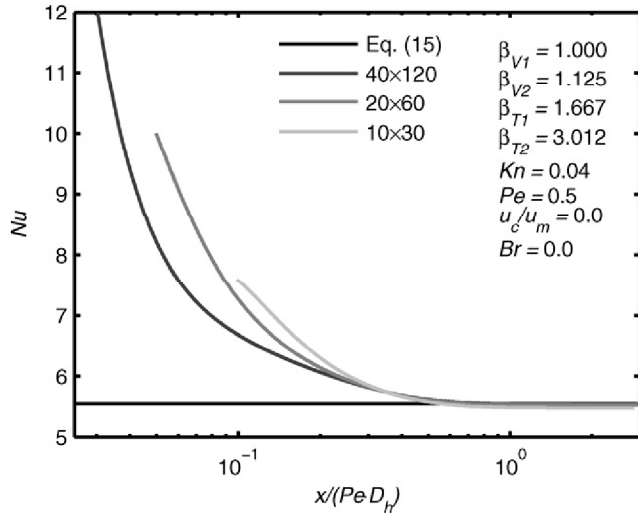
Fig. 2. Grid dependence data.

Table 2
Conditions for the grid dependence study

Grid resolution	Nu_∞	ε_{Nu_∞}	Po_∞	ε_{Po_∞}	Time
Eq. (13) or (15)	5.550	–	61.287	–	–
40×120	5.545	−0.08%	61.238	−0.08%	116 h
20×60	5.533	−0.31%	61.092	−0.32%	3.75 h
10×30	5.482	−1.23%	60.515	−1.26%	0.75 h
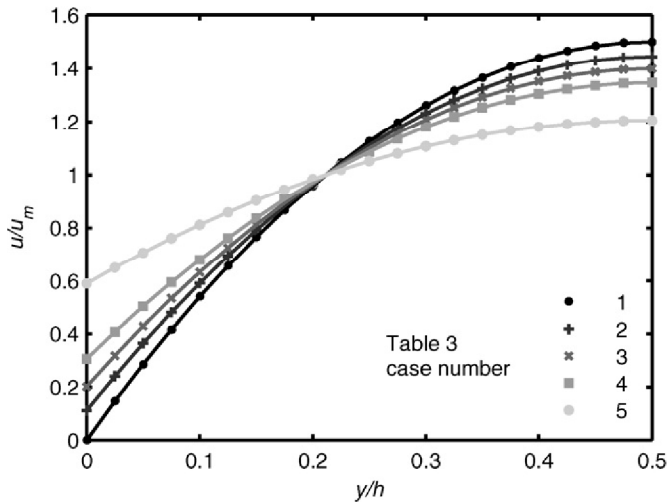
Fig. 3. Analytical and numerical velocity profiles.

3.3. Code verification

To verify that the numerical algorithm accurately models the effects of the various slip boundary conditions, creep velocity, and viscous dissipation the analytically and numerically computed fully developed velocity and temperature profiles are compared in Figs. 3 and 4 for the flow conditions specified in Table 3. The nondimensional velocity profiles are given in Fig. 3, where the symbols represent the numerically computed values and the lines represent the analytic solution, Eq. (11). The nondimensional temperature profiles are pre-
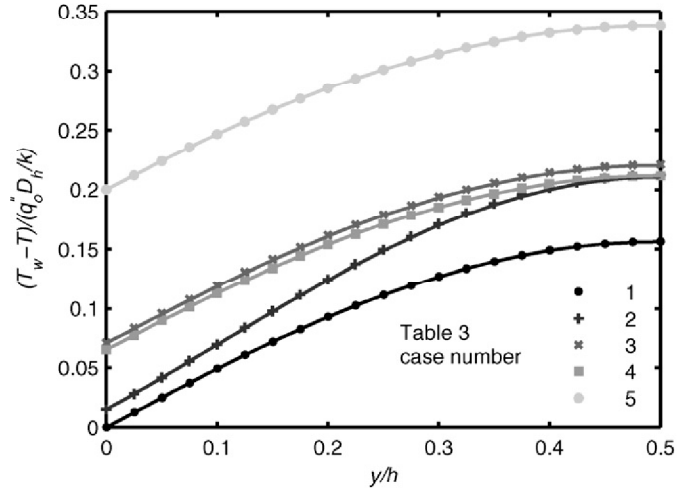

Fig. 4. Analytical and numerical temperature profiles.

Table 3
Conditions for comparison of analytical and numerical velocity and temperature profiles

Case number	Boundary condition	β_{V1}	β_{T1}	Kn	$\frac{u_c}{u_m}$	Br
1	no slip	1.0	1.667	0.00	0.00	0.00
2	second-order [16]	1.0	1.667	0.01	0.00	0.05
3	second order [16]	1.0	1.667	0.04	0.25	0.00
4	second-order [17]	1.0	1.667	0.04	0.00	0.00
5	first-order [14,15]	1.0	1.667	0.12	0.00	0.00

sented in Fig. 4, where the lines again represent the analytic solutions, Eq. (14). The differences between the numerically and analytically computed values are negligible.

4. Results and discussion

In the following presentation of the numerical and analytical results Po and Nu are normalized by their continuum values, which are 96 and 8.235, respectively. Also, to reduce the number of variables involved, the nondimensional parameters, $\beta_{V1}Kn$ and β_{T1}/β_{V1}, introduced by Larrode et al. [4], will be used. $\beta_{V1}Kn$ represents the level of rarefaction, with $\beta_{V1}Kn = 0$ corresponding to continuum conditions. The ratio β_{T1}/β_{V1} represents the gas-wall interactions, and may range from 0 to more than 100. $\beta_{T1}/\beta_{V1} = 1.667$ corresponds to typical properties for air when $\sigma_V = \sigma_T = 1$. $\beta_{T1}/\beta_{V1} = 0$ corresponds to the artificial condition of a no temperature jump boundary condition while there is a slip velocity boundary condition. It should be noted that when second-order Deissler boundary conditions are used either analytically or numerically, if $\beta_{T1} = 0$ then β_{T2} is also taken to be zero, although this is not explicitly stated in the boundary conditions presented in Eq. (4). Also, although it has been verified that the algorithm accurately models flows with viscous dissipation (Table 3, case number 2), by comparison to Eqs. (11) and (14), numerical results that include viscous dissipation will not be presented here so that second-order effects and creep flow effects may be seen more clearly.
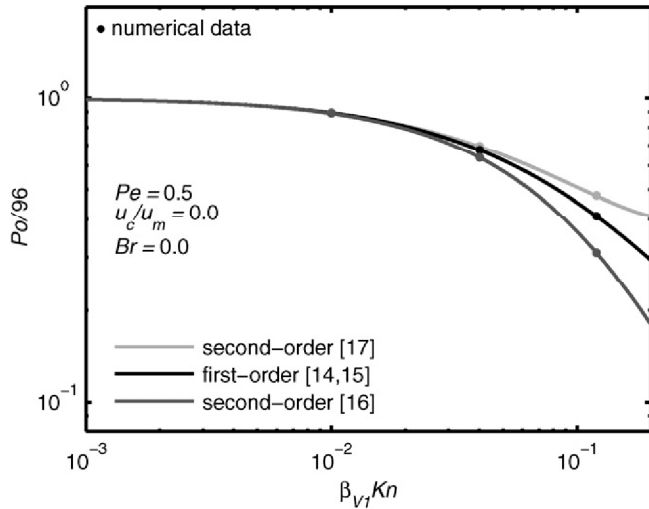
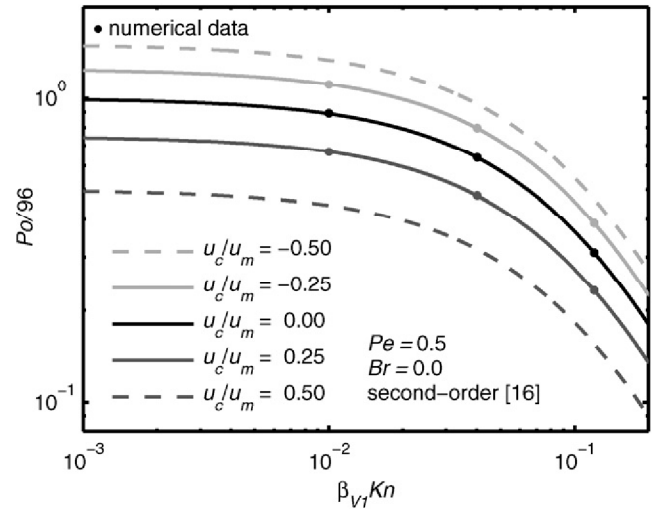Fig. 5. Effect of slip boundary conditions on fully developed Po.

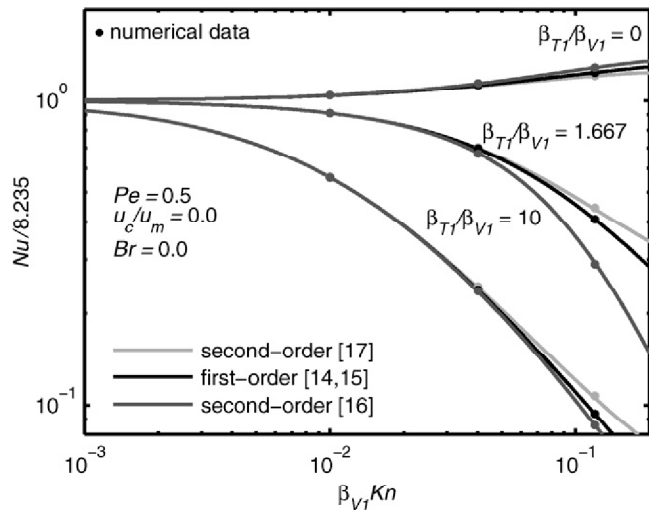

Fig. 7. Effect of creep velocity on fully developed Po.

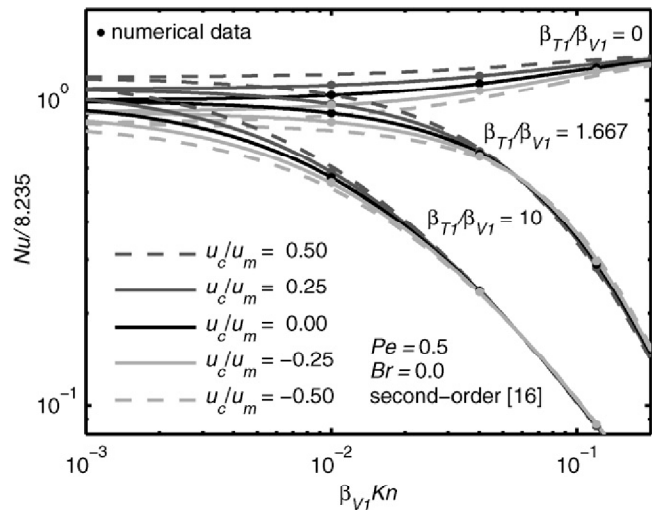Fig. 6. Effect of slip boundary conditions on fully developed Nu.

Fig. 8. Effect of creep velocity on fully developed Nu.

4.1. Fully developed Po and Nu

The numerical results for fully developed flows are compared to the analytically derived Po and Nu in Figs. 5–8. The numerical data are given by the symbols, and the analytic solutions are represented as lines. The average difference between the analytic Po, Eq. (13), and the numerical Po is 0.06%, and the maximum difference is 0.70%. The average difference between the analytic Nu, Eq. (15), and the numerical Nu is 0.33%, and the maximum difference is 1.72%.

The comparison of the resulting Po, when using first-order [14,15], second-order Deissler [16], or second-order Karniadakis and Beskok [17] boundary conditions is given in Fig. 5. A similar comparison for Nu is given in Fig. 6. For these data, creep flow and viscous dissipation effects are neglected, and $Pe = 0.5$. The data in Fig. 5 illustrate that as rarefaction, $\beta_{V1}Kn$, increases, the slip velocity increases, which results in a flatter velocity profile with reduced wall velocity gradients (as shown in Fig. 3) and consequently decreases Po. The increased slip flow at the wall, due to increasing rarefaction also

amplifies the energy exchange near the wall which tends to increase Nu, as seen when $\beta_{T1}/\beta_{V1} = 0$ in Fig. 6. However, when $\beta_{T1}/\beta_{V1} \neq 0$, rarefaction increases the temperature jump at the wall as well as the slip velocity, which reduces the energy exchange and results in a shift in the temperature distribution (as shown in Fig. 4) which increases the mean temperature difference and consequently tends to decrease Nu. These results are consistent with previous first-order slip results [4,8] and indicate that slip decreases Po, and may either increase or decrease Nu depending on the magnitude of $\beta_{V1}Kn$ and β_{T1}/β_{V1}.

The results presented in Figs. 5 and 6 also indicate that second-order slip terms become more significant as rarefaction, $\beta_{V1}Kn$, increases. However, it is important to observe that the two second-order models have opposite effects when compared to the first-order boundary condition data. This result is expected, due to the opposite signs of the second-order coefficients, given in Table 1. The second-order Deissler coefficients are positive, which result in an increase in both the slip velocity and the temperature jump for increasing rarefaction, while the second-order Karniadakis and Beskok coefficients are negative,

which result in a decrease for both the slip velocity and the temperature jump for increasing rarefaction. At $\beta_{V1}Kn = 0.12$ and $\beta_{T1}/\beta_{V1} = 1.667$, the second-order Deissler boundary conditions predict a 24.2% decrease in Po and a 28.0% decrease in Nu, as compared to the first-order boundary conditions, while the Karniadakis and Beskok boundary conditions predict a 16.5% increase in Po and a 8.2% increase in Nu, as compared to the first-order boundary conditions.

The effect of creep velocity on Po and Nu is shown in Figs. 7 and 8, respectively. For these data, viscous dissipation effects are neglected, second-order Deissler boundary conditions are used, and $Pe = 0.5$. The data in Fig. 7 indicate that creep flow in the same direction as the mean flow, positive u_c/u_m, increases the total slip velocity, which flattens the velocity profile and reduces Po. Conversely, creep flow in the opposite direction of the mean flow, negative u_c/u_m, decreases the total slip velocity at the wall, which increases the wall velocity gradient, thereby increasing Po.

There are several factors that contribute to the creep flow effect on Nu, as presented in Fig. 8. Creep flow in the same direction as the mean flow increases the total slip velocity, which increases the energy exchange near the wall and tends to increase Nu. Creep flow in the opposite direction of the mean flow decreases the total slip velocity, which decreases the energy exchange near the wall and tends to decrease Nu. This creep flow effect on Nu is seen most clearly for the lower $\beta_{V1}Kn$ values of Fig. 8. However, as rarefaction increases, the effect of the increasing temperature jump at the wall (for $\beta_{T1}/\beta_{V1} \neq 0$), and the decreasing velocity gradients decrease the energy exchange, which reduces Nu, as well as the effect of u_c/u_m on Nu. As rarefaction increases even further, the second-order effects become more significant. The second-order contribution to the temperature distribution, the last term of Eq. (14), is a function of the second-order temperature jump coefficient, β_{T2}, rarefaction, Kn^2, the total slip velocity, u_s/u_m, and the viscous dissipation, Br ($Br = 0$ for these calculations). Creep flow in the same direction as the mean flow increases the total slip velocity, thereby increasing the second-order effect on the temperature jump; whereas, creep flow in the opposite direction of the mean flow decreases the overall slip velocity, thereby decreasing the second-order effect on the temperature jump. For the second-order Deissler boundary conditions, which are used for the analysis in Fig. 8, this causes the lines of positive and negative u_c/u_m to cross at high $\beta_{V1}Kn$ (for $\beta_{T1}/\beta_{V1} \neq 0$). While not shown, neither the first-order, nor the second-order Karniadakis and Beskok boundary conditions with creep flow result in this effect at high $\beta_{V1}Kn$.
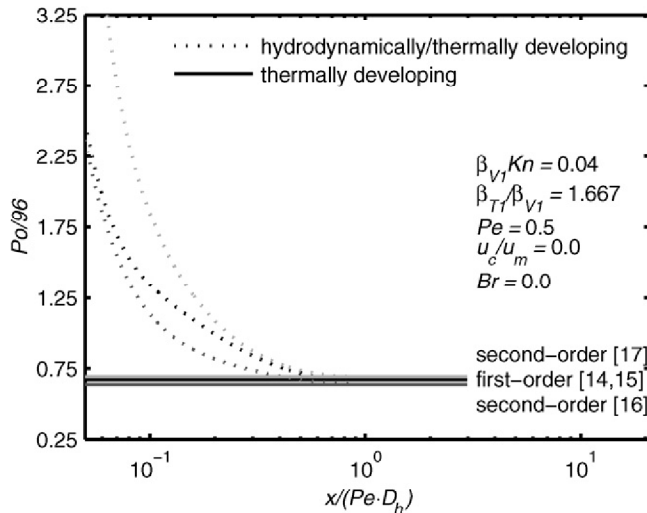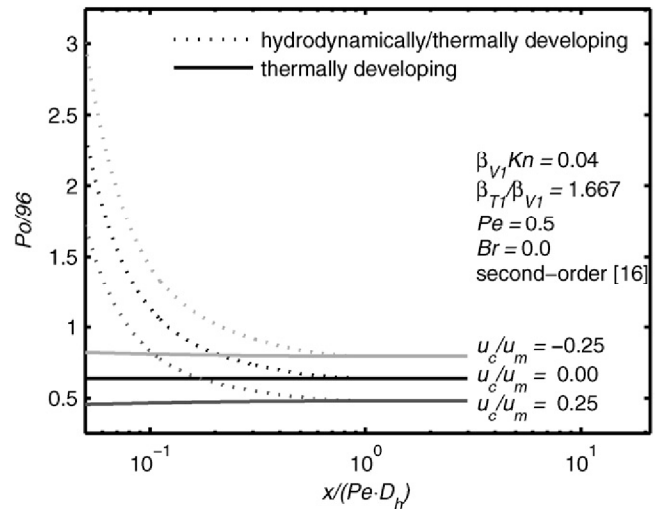
4.2. Entrance Po and Nu

Comparisons of numerically computed Po and Nu for thermally developing and combined hydrodynamically/thermally developing flow for the various slip boundary condition models and u_c/u_m are given in Figs. 9–12. Each figure displays the flow parameters used in the numerical model, with all of the hydrodynamically/thermally developing solutions represented by a dashed line, and all of the thermally developing solutions represented with a solid line. For the thermally developing solutions, the flow is hydrodynamically fully developed at the entrance, which results in a constant Po through the length of the channel. In general, all of the combined hydrodynamically/thermally developing Po and Nu are initially larger than the thermally developing Po and Nu, due to the larger velocities and velocity gradients at the wall. However, as the flows develop, the thermally and the combined hydrodynamically/thermally developing values converge to the fully developed values of Po and Nu which correspond to the data presented in Figs. 5–8. The effects of $\beta_{V1}Kn$ and β_{T1}/β_{V1} on thermally developing flow have been presented in previous studies [8], and so will not be presented here. However, these results are as would be expected based on the fully developed results. Increasing $\beta_{V1}Kn$, results in decreasing Po and Nu for both the entrance and the fully developed values, and increasing β_{T1}/β_{V1} results in decreasing Nu for both the entrance and fully developed values.

The data in Figs. 9 and 10 demonstrate the effect of the different slip boundary condition models through the thermal and combined hydrodynamic/thermal entrance lengths of Po and Nu, respectively. Just as in the fully developed case, Deissler boundary conditions generally predict lower Po and Nu values compared to the first-order model, and Karniadakis and Beskok boundary conditions predict higher Po and Nu values compared to the first-order model. The differing second-order effects, due to the opposite signs of the second-order coefficients given in Table 1, are even more significant at the channel entrance than for the fully developed values, due to the large first- and second-order velocity and temperature gradients at the channel entrance.

The effects of creep velocity on the thermal and combined hydrodynamic/thermal entrance length Po and Nu are shown in Figs. 11 and 12, respectively. For these results second-order Deissler boundary conditions are used. As in the fully developed case at $\beta_{V1}Kn = 0.04$, creep velocity in the same direction as the mean velocity reduces Po and increases Nu, while creep flow opposite to the mean flow increases Po and decreases Nu, compared to the case where creep flow is not considered. Close examination of Fig. 11 will reveal that the thermally developing Po curves that include creep flow are not perfectly horizontal; Po with negative creep flow decreases slightly, while Po with positive creep flow increases slightly. This is because the creep velocity contribution to the inlet flow is coupled to the thermal development and as such cannot be truly hydrodynamically fully developed until it is also thermally fully developed. At the channel entrance, before the constant axial temperature gradient is established, Nu for each of the three thermally developing flows is approximately the same value, and Nu for each of the three hydrodynamically/thermally developing flows is approximately the same value. As the axial temperature gradient and resulting creep velocity becomes constant, the Nu data that include creep flow diverge from Nu with no creep flow and approach the fully developed Nu values which are dependent on u_c/u_m.

Fig. 9. Effect of slip boundary conditions on entrance *Po*.

Fig. 11. Effect of creep velocity on entrance *Po*.
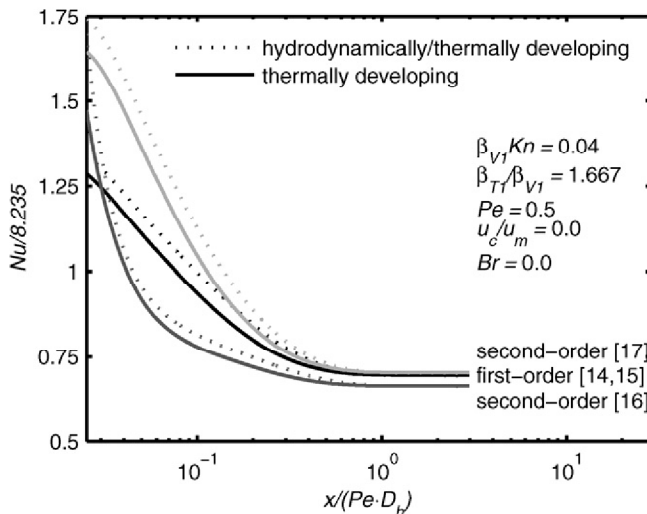
Fig. 10. Effect of slip boundary conditions on entrance *Nu*.
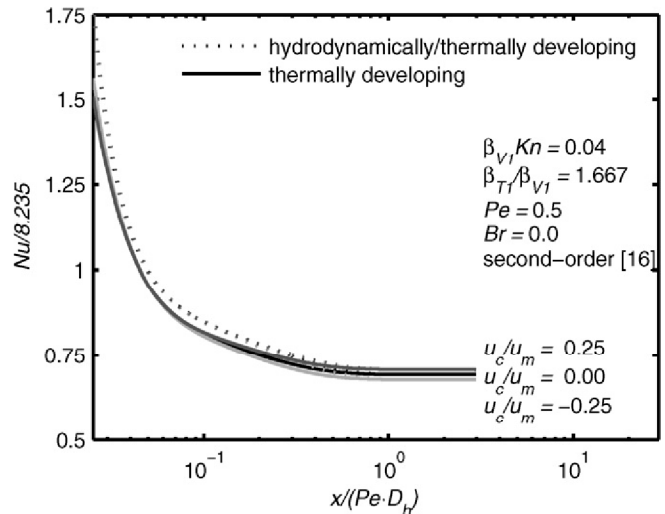
Fig. 12. Effect of creep velocity on entrance *Nu*.

5. Conclusions

The Poiseuille and Nusselt numbers of two-dimensional constant wall heat flux flows in the slip regime have been calculated both analytically and numerically using second-order slip and temperature jump boundary conditions. The analytical equations for *Po* and *Nu* are expressed in terms of the degree of rarefaction (Kn); the slip flow model parameters β_{V1}, β_{V2}, β_{T1}, and β_{T2}; the creep flow (u_c/u_m); and the amount of viscous dissipation (Br). The analytic solutions are valid for nearly incompressible, steady state, and hydrodynamically/thermally fully developed flows. Numerical solutions for microchannel *Po* and *Nu* are calculated using a continuum based three-dimensional, unsteady, compressible, CFD algorithm modified with slip boundary conditions. For fully developed flows the differences between numerically and analytically computed *Po* and *Nu* are negligible. With the numerical algorithm verified, it is then used to evaluate hydrodynamically/thermally developing *Po* and *Nu*.

Both analytical and numerical data indicate that second-order terms and creep velocity effects are significant within the slip flow regime. This study quantifies the effects of two second-order models [16,17]; however, the analytic solutions may be used for any second-order slip model with boundary conditions of the same general form. This variability is important due to the lack of experimental data and agreement on second-order boundary conditions. The significance of including creep flow in the analytical or numerical analysis of *Po* and *Nu* depends on the magnitude of the heat flux and the degree of rarefaction.

References

[1] R.M. Inman, Laminar slip flow heat transfer in a parallel-plate channel or a round tube with uniform wall heating, NASA TN D-2393 (1964).

[2] T.A. Ameel, X. Wang, R.F. Barron, R.O. Warrington, Laminar forced convection in a circular tube with constant heat flux and slip flow, Microscale Thermophysical Engineering 1 (1997) 303–320.

[3] R.F. Barron, X. Wang, T.A. Ameel, R.O. Warrington, The Graetz problem extended to slip-flow, International Journal of Heat and Mass Transfer 40 (1997) 1817–1823.

[4] F.E. Larrode, C. Housiadas, Y. Drossinos, Slip-flow heat transfer in circular tubes, International Journal of Heat and Mass Transfer 43 (2000) 2669–2680.

[5] G. Tunc, Y. Bayazitoglu, Heat transfer for gaseous flow in microtubes with viscous heating, American Society of Mechanical Engineers, Heat Transfer Division, (Publication) HTD 366 (2000) 299–306.

[6] G. Tunc, Y. Bayazitoglu, Convection at the entrance of micropipes with sudden wall temperature change, American Society of Mechanical Engineers, Heat Transfer Division, (Publication) HTD 372 (2002) 265–270.

[7] X. Chen, B. Xu, The Nusselt number and friction factor at the entrance of a micro-duct, International Communications in Heat and Mass Transfer 29 (2002) 763–772.

[8] S. Yu, Slip flow heat transfer in rectangular microchannels, Ph.D. thesis, University of Utah, USA, 2002.

[9] N.G. Hadjiconstantinou, Convective heat transfer in micro and nano channels: Nusselt number beyond slip flow, American Society of Mechanical Engineers, Heat Transfer Division, (Publication) HTD 366 (2000) 13–22.

[10] N.G. Hadjiconstantinou, O. Simek, Constant-wall-temperature Nusselt number in micro and nano-channels, Journal of Heat Transfer 124 (2002) 356–364.

[11] N.G. Hadjiconstantinou, The effect of viscous heat dissipation on convective heat transfer in small-scale slipping gaseous flows, International Conference on Microchannels and Minichannels 1 (2003) 269–273.

[12] H.P. Kavehpour, M. Faghri, Y. Asako, Effects of compressibility and rarefaction on gaseous flows in microchannels, Numerical Heat Transfer; Part A: Applications 32 (1997) 677–696.

[13] C.S. Chen, W.J. Kuo, Heat transfer characteristics of gaseous flow in long mini- and microtubes, Numerical Heat Transfer; Part A: Applications 46 (2004) 497–514.

[14] J.C. Maxwell, On stresses in rarified gases arising from inequalities of temperature, Philosophical Transactions of the Royal Society, London 170 (1879) 231–256.

[15] M. Smoluchowski, Ueber wärmeleitung in verdünnten gasen, Annalen der Physik und Chemie 64 (1898) 101–130.

[16] R.G. Deissler, An analysis of second-order slip flow and temperature-jump boundary conditions for rarefied gases, International Journal of Heat and Mass Transfer 7 (1964) 681–694.

[17] G.E. Karniadakis, A. Beskok, Micro Flows: Fundamentals and Simulation, Springer-Verlag, New York, 2002.

[18] J. Maurer, P. Tabeling, P. Joseph, H. Willaime, Second-order slip laws in microchannels for helium and nitrogen, Physics of Fluids 15 (2003) 2613–2621.

[19] S. Colin, P. Lalonde, R. Caen, Validation of a second-order slip flow model in rectangular microchannels, Heat Transfer Engineering 25 (2004) 23–30.

[20] R.K. Shah, A.L. London, Laminar Flow Forced Convection in Ducts, Academic Press, New York, 1978.

[21] F. Harlow, A. Amsden, Numerical calculation of almost incompressible flow, Journal of Computational Physics 3 (1968) 80–93.

[22] B. Kashiwa, R. Rauenzahn, A cell-centered ICE method for multiphase flow simulations, Los Alamos National Laboratory Technical Report LA-UR-93-3922 (1994).

[23] J.E. Guilkey, T. Harman, A. Xia, B. Kashiwa, P. McMurtry, An Eulerian-Lagrangian approach for large deformation fluid structure interaction problems, Part 1: Algorithm development, Advances in Fluid Mechanics, Fluid Structure Interaction II 36 (2003) 143–156.

[24] T. Harman, J.E. Guilkey, B. Kashiwa, J. Schmidt, P. McMurtry, An Eulerian-Lagrangian approach for large deformation fluid structure interaction problems, Part 2: Multi-physics simulations within a modern computational framework, Advances in Fluid Mechanics, Fluid Structure Interaction II 36 (2003) 157–166.

[25] S.G. Parker, J. Guilkey, T. Harman, A component-based parallel infrastructure for the simulation of fluid-structure interaction, Engineering with Computers 22 (2006) 277–292.